separations

MDPI

Article

A Novel Hybrid Adsorbent Based on Fly Ash and Waste Flax Fibers for Efficient Separation of Rare Earth Ions from Water

Tijana Radojičić [1], Katarina Trivunac [1,*], Marina Maletić [2], Ivona Janković-Častvan [1], Miloš Simić [3], Ana Kalijadis [3] and Marija Vukčević [1]

[1] Faculty of Technology and Metallurgy, University of Belgrade, Karnegijeva 4, 11120 Belgrade, Serbia; radojicic.tijana96@gmail.com (T.R.); icastvan@tmf.bg.ac.rs (I.J.-Č.); marijab@tmf.bg.ac.rs (M.V.)
[2] Innovation Center, Faculty of Technology and Metallurgy, Karnegijeva 4, 11120 Belgrade, Serbia; mvukasinovic@tmf.bg.ac.rs
[3] "VINČA" Institute of Nuclear Sciences—National Institute of the Republic of Serbia, University of Belgrade, Mike Petrovica Alasa 12–14, 11000 Belgrade, Serbia; milos.simic@vin.bg.ac.rs (M.S.); ana.kalijadis@vin.bg.ac.rs (A.K.)
* Correspondence: trivunac@tmf.bg.ac.rs

Abstract

In this study, carbonaceous and hybrid adsorbents were synthesized from waste flax fibers and fly ash, integrating two abundant waste streams into a single functional material. Materials were thermally modified and activated with NaOH at 500 °C in a nitrogen atmosphere. The prepared adsorbents exhibit high efficiency for scandium ion removal, with the hybrid systems significantly outperforming the individual components. The obtained Langmuir maximum adsorption capacities for the adsorption of scandium onto hybrid adsorbents were 18.28 and 32.32 mg/g, depending on the flax fibers/fly ash ratio. The contrasting thermodynamic behavior between hybrid adsorbents of different composition highlights the significant influence of material structure on the adsorption mechanism. The results demonstrate that the synergistic integration of waste flax fibers and fly ash in hybrid materials produces efficient and environmentally sustainable adsorbents, offering a novel approach for REE recovery from aqueous systems.

Keywords: hybrid adsorbent; rare earth elements; fly ash; waste flax fibers; water treatment

1. Introduction

Rare earth elements (REEs) are key resources in the transition to a sustainable low-carbon economy due to their unique magnetic, catalytic and luminescent properties [1,2]. They are widely used in advanced technologies, including electronic devices, high-performance magnets, electric vehicles and wind turbines. However, conventional extraction of REEs from primary ores is associated with high energy consumption and intensive use of hazardous chemicals, resulting in a significant environmental impact. Consequently, increasing attention has been focused on alternative sources of REEs, such as mining residues [3], electronic waste [4] and coal-derived by-products [5,6], in accordance with the principles of the circular economy [7]. Among the available recovery techniques, adsorption has emerged as an effective and environmentally friendly approach for the removal and recovery of REEs from dilute aqueous solutions due to its simplicity of operation, low energy requirements, and high efficiency. A wide range of materials, including carbon-based adsorbents, aluminosilicates, metal oxides, and biosorbents, have been investigated for this purpose. In recent years, hybrid and composite materials [2,7–9]

Check for updates

Academic Editor: Xinhua Qi

Received: 20 March 2026
Revised: 24 April 2026
Accepted: 28 April 2026
Published: 1 May 2026

Copyright: © 2026 by the authors. Licensee MDPI, Basel, Switzerland. This article is an open access article distributed under the terms and conditions of the Creative Commons Attribution (CC BY) license.

have received considerable attention as a strategy to overcome the limitations of single adsorbents. By combining organic, inorganic, and waste-derived components [10,11], these materials can achieve synergistic improvements in porosity, surface chemistry, and structural stability. In particular, coal ash-based hybrids have been widely investigated due to their low cost and abundance of ash, as well as their intrinsic aluminosilicate composition. However, raw fly ash usually shows a limited adsorption capacity for metals [12] due to its small specific surface area and insufficient density of active sites, which requires further modification. Various approaches have been proposed to improve the performance of ash-based adsorbents [13–20]. In general, most existing hybrid systems achieve only partial optimization of key properties, such as porosity, surface functionality and structural stability. To address these challenges, hybrid materials obtained by co-processing lignocellulosic biomass and fly ash via thermal and chemical activation have emerged as promising candidates. Pyrolysis-based materials, including biochar, are known for their large surface area and tunable porosity; however, their properties strongly depend on the pyrolysis conditions (temperature, heating rate, residence time), which leads to variability in structure and surface functionality [21,22]. In contrast, the integration of biomass-derived carbon with fly ash mineral phases offers the possibility of combining high porosity with ion exchange capacity and mechanical stability. While various types of biomasses have been explored for the synthesis of fly ash-based hybrid materials, to the best of our knowledge, the utilization of flax fiber as a carbonaceous precursor remains unexplored in the existing literature. In this context, the use of flax fiber as a lignocellulosic precursor presents clear advantages compared to other common lignocellulosic materials such as wood or agricultural residues [23,24]. During NaOH activation, wood needs significant energy to break down the higher lignin content and reach the inner cellulose [25]. Wood biochars at 500 °C start to lose oxygen groups as they become more aromatic (graphitic). Furthermore, they often have large, irregular macropores. Agricultural wastes such as straw, husk, and bagasse have a high ash content and a high hemicellulose content, but a lower cellulose content than flax [26–29]. At 500 °C, hemicellulose rapidly decomposes, often leading to a collapsed pore structure. The high initial cellulose content and high availability of hydroxyl groups in flax [30] increase its reactivity towards alkaline activation, which leads to an increased density of oxygen-containing functional groups that act as active REE binding sites. Flax is naturally low in ash, resulting in a "cleaner" carbon phase intended to bind functional groups. Flax fibers have a high aspect ratio (length to width), which allows NaOH to penetrate and more evenly etch the surface. The moderate content of lignin in flax (2–5%), distributed between layers of cellulose, allows NaOH to create a hierarchical pore structure (both micro and meso), which allows REEs to travel rapidly deep into the adsorbent [31]. The synthesis of a novel hybrid adsorbent via pyrolysis at 500 °C in an inert atmosphere from a mixture of fly ash, flax fibers, and NaOH represents the main objective of this study. In such a system, flax-derived carbon provides a porous matrix with oxygen-containing functional groups, while fly ash contributes to structural stability and ion-exchange capacity. Sodium hydroxide plays a multifunctional role by promoting chemical activation, enhancing surface reactivity, and enabling partial geopolymerization of the inorganic phase. The synthesis conditions, including the temperature of 500 °C and the use of a 5 M NaOH solution, were selected based on literature data as moderate conditions that allow partial carbonization of lignocellulosic biomass while retaining functional groups, as well as sufficient activation of the fly ash component. These parameters were not subject to systematic optimization in this study, but were kept constant in order to isolate the effect of the composition of the starting mixture on the properties and adsorption performance of the obtained materials. The synergistic integration of these components is expected to result in a multifunctional adsorbent with enhanced active site accessibility,

improved diffusion through a hierarchical pore structure, and strong interactions with REE ions governed by Lewis acid–base chemistry. Consequently, the developed hybrid material is expected to show good adsorption performance towards REEs, emphasizing its potential for sustainable applications in water purification and resource recovery.

2. Materials and Methods

2.1. Material

The fly ash utilized in this research was generated during coal combustion at the Thermal Power Plant Nikola Tesla B, located in Obrenovac, Serbia, and flax fibers were purchased from Naturaland, Ljubljana, Slovenia. The chemicals used for material modification and adsorption experiments were sodium hydroxide (pellets, ≥97%, CAS No: 1310-73-2) and hydrochloric acid (37%, CAS No: 7647-01-0), supplied by Sigma-Aldrich (St. Louis, MO, USA). The stock solutions (1.00 g dm^{-3}) of the elements for the adsorption test were prepared from the salts Y^{3+} ($Y(NO_3)_3 \cdot 6H_2O$, 99.8%, CAS No: 13494-98-9), Sc^{3+} (solution of $Sc(NO_3)_3 \cdot H_2O$, 99.9%, CAS No: 107552-14-7), and Gd^{3+} (solution of $Gd(NO_3)_3 \cdot 6H_2O$, 99.99%, CAS No: 19598-90-4), also purchased from Sigma-Aldrich (St. Louis, MO, USA).

2.2. Sample Preparation

Carbonaceous and hybrid adsorbents were prepared using flax fibers and fly ash as starting materials. Material mixtures were subjected to thermal treatment in an electrical furnace at 500 °C under N_2 atmosphere, with a heating rate of 5 °C/min, using NaOH solution as an activating agent (solid-to-liquid ratio was 1:3). Flax fibers were mixed with 5 M NaOH, and the homogenized mixture was subjected to thermal treatment. In this way, the sample marked L was obtained. For the preparation of hybrid adsorbents L_1/FA_1 and L_2/FA_1, flax fibers and fly ash, in the mass ratios of 1:1 and 2:1, respectively, were also mixed with 5 M NaOH, homogenized, and thermally treated. Following carbonization and activation, samples were washed with distilled water to reach a neutral pH and dried at 60 °C overnight. All synthesis parameters were kept constant throughout the study and were not systematically varied, as the focus was on evaluating the influence of the flax fibers/fly ash ratio rather than on optimization of synthesis conditions.

2.3. Material Characterization

The morphology of the obtained samples was examined using field emission scanning electron microscopy (FESEM, Mira3, Tescan Orsay Holding, Brno, Czech Republic), operating at 20 eV. Before analysis, the samples were sputter-coated with a thin gold layer to ensure adequate surface conductivity.

Nitrogen adsorption–desorption isotherms were measured at the temperature of liquid nitrogen (77 K) using a Micromeritics ASAP 2020 surface area and porosity analyzer (Micromeritics N.V./S.A., Brussels, Belgium). Prior to analysis, the samples were degassed under vacuum to remove physically adsorbed impurities and moisture. The specific surface area (S_{BET}) was calculated according to the Brunauer–Emmett–Teller (BET) method. In addition, the total pore volume (V_{total}), mesopore volume (V_{meso}), micropore volume (V_{micro}), and D_{max}—pore size at maximum pore volume—were determined using the ASAP 2020 software package.

The crystalline structure of the investigated materials was analyzed by X-ray diffraction (XRD) using a Proto AXRD Benchtop diffractometer, LaSalle, ON, Canada, with Bragg–Brentano geometry and a CuKα radiation source (λ = 0.154 nm) in the 2θ angle range from 5° to 70° and a scanning rate of 1 °/min.

Surface functional groups of the materials were identified by Fourier transform infrared spectroscopy (FTIR) using a Nicolet™ iS™ 10 FT-IR Spectrometer (Thermo Fisher

Scientific, Waltham, MA, USA) with Smart iTR™ Attenuated Total Reflectance (ATR) Sampling accessories. Spectra were collected in the wavenumber range from 4000 to 500 cm^{-1} with a resolution of 4 cm^{-1}.

The point of zero charge (pH_{PZC}) of the studied materials was determined using the pH drift method. Briefly, 0.06 g of each sample was dispersed in 20 cm^3 of 0.01 M KCl solution, with the initial pH (pHi) adjusted to values of 2, 4, 6, 8, 10, and 12 by addition of 0.1 M HCl or 0.1 M NaOH. The suspensions were purged with nitrogen, sealed, and maintained under continuous shaking at room temperature for 48 h to reach equilibrium. Subsequently, the final pH (pH_f) was measured, and the pH_{PZC} was obtained from the intersection point of the ΔpH versus pHi curve and the *x*-axis [32].

The thermogravimetric (TG) analysis was performed on an SDT Q600 instrument (TA Instruments, New Castle, DE, USA) in an air atmosphere (flow rate: 100 cm^3/min; heating rate: 20 °C/min), ranging from room temperature to 800 °C.

2.4. Adsorption Experiments

All adsorption experiments were conducted in a batch system under constant agitation (150 rpm) at room temperature, using 0.05 g of adsorbent and 20 cm^3 of aqueous REE solutions (scandium, yttrium, and gadolinium). The influence of fly ash presence in the starting material for adsorbent preparation on its adsorption efficiency was examined through the adsorption of REEs from the multi-element solution (initial concentration of each element: 10 mg dm^{-3}). The adsorption of REEs from a multi-element solution onto hybrid adsorbents was optimized by examining the effects of contact time, initial pH, initial REE concentration, and temperature. The effect of the initial pH value on adsorption onto hybrid adsorbents (adsorbent mass-to-adsorbate volume ratio: 2.5 g/dm^3) was investigated by adjusting the pH of the REE solution (10 mg dm^{-3}) to values of 2.0, 2.5, 3.0, 3.5, and 4.0 (±0.01) using diluted HCl or NaOH solutions. Based on the adsorption efficiencies obtained at different pH values of the adsorbate solution and the REE speciation (obtained using Visual Minteq 3.1 software), the optimal initial pH was selected. The influence of contact time was evaluated by adsorption from REE solution (adsorbent mass-to-adsorbate volume ratio: 2.5 g/dm^3) at an initial concentration of 25 mg dm^{-3}. The concentrations of REEs during this adsorption experiment were examined at predetermined time intervals (10, 30, 60, 120, 180, 360, 720, 1440, and 2880 min), using Inductively Coupled Plasma Optical Emission Spectroscopy (ICP-OES, Agilent, Santa Clara, CA, USA). Furthermore, the effect of the initial concentration on adsorption capacity was studied using REE solutions at different concentrations (7.5, 10, 15, 20, 25, 30, 50, 75, and 100 mg dm^{-3}) and an adsorbent mass-to-adsorbate volume ratio of 2.5 g/dm^3. The effect of temperature on adsorption performance was examined using REE solution at an initial concentration of 15 mg dm^{-3} at three different temperatures: 25, 35, and 45 °C, whereby the adsorbent mass-to-adsorbate volume ratio was the same as in previous experiments. Based on the obtained results, thermodynamic parameters were calculated using equations given in Table S1 (Supplementary Materials). The obtained experimental adsorption data were interpreted using kinetic and equilibrium models, including pseudo-first-order, pseudo-second-order, and Elovich kinetic models, as well as the intraparticle diffusion model for adsorption kinetics. Equilibrium adsorption data were analyzed using the Langmuir, Freundlich, Dubinin–Radushkevich, and Temkin adsorption isotherms. Equations of the theoretical models used to analyze the obtained adsorption data are given in Table S1.

3. Results and Discussion

3.1. Material Characterization

The morphology of the obtained samples was analyzed by scanning electron microscopy (Figure 1), which revealed distinct morphological features of thermally treated flax fibers and the hybrid adsorbents. Carbonaceous material obtained by activation of flax fibers (Figure 1a) is characterized by a highly porous, sponge-like structure with an interconnected network of pores of different sizes. The thin pore walls that look like nanosheets indicate extensive decomposition of the lignocellulosic matrix during thermal treatment, which may lead to a high specific surface area. The morphology of hybrid adsorbent L_1/FA_1 (Figure 1b) combines a heterogeneous and partially densified structure, originating from a porous carbon phase (flax origin) and a mineral phase (fly ash origin). The carbon phase retains its porous sponge-like morphology, while the mineral component appears more compact and granular, characteristic of aluminosilicate materials. A higher magnification of the fly ash origin phase of sample L_1/FA_1 revealed a rough and slightly porous surface. The surface of hybrid adsorbent L_2/FA_1 (Figure 1c) contains numerous spherical particles with a rough surface, originating from fly ash, embedded within the porous carbon matrix. These particles completely cover the surface of the carbonaceous phase of the hybrid adsorbent and block its pores. The morphologies of hybrid adsorbents are characterized by enhanced structural heterogeneity, which may be advantageous for adsorption applications.

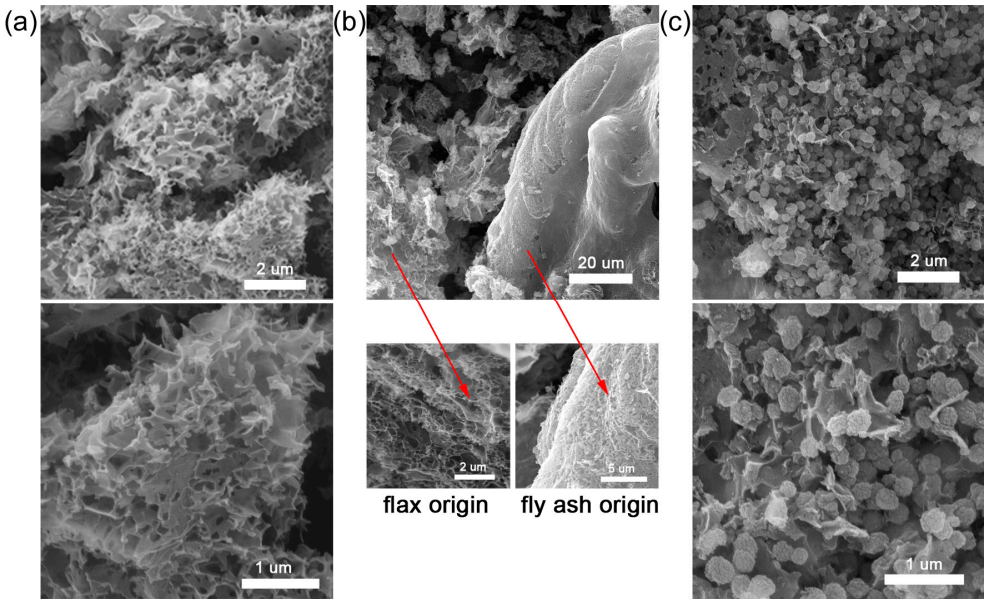


Figure 1. SEM photographs of samples (**a**) L, (**b**) L_1/FA_1, and (**c**) L_2/FA_1.

Textural properties of carbonaceous flax fibers and hybrid adsorbents are given in Table 1, and pore size distribution is given in Figure 2. All examined samples are mesoporous, with the highest specific surface area of 59.05 m^2/g, obtained for sample L. As a lignocellulosic material, flax fibers can be successfully converted into carbon materials with a well-developed specific surface area [33,34] if a high activation temperature and a sufficient amount of activating agent are used. The parameters used for preparation of the L sample and hybrid adsorbents were not that severe, and flax fibers were not completely converted to carbon material with developed porosity. The presence of fly ash in the starting mixture decreases the specific surface area; the higher the amount of fly ash, the lower the specific surface area is. It is reported in the literature [35] that this kind of modification of biochar considerably decreases the surface area due to the blocking of pores

by fly ash. This observation is further supported by the reduction in total pore volume (V_{total}) with increasing fly ash content. As can be seen from Figure 2 and the D_{max} values (Table 1), the average pore diameter for all samples is around 4 nm, indicating that this porosity originates from the flax component.

Table 1. Textural properties of samples L, L_1/FA_1 and L_2/FA_1.

Material	S_{BET}, m^2/g	V_{total}, cm^3/g	V_{meso}, cm^3/g	V_{micro}, cm^3/g	D_{max}, nm
L	59.05	0.1634	0.1399	0.0202	3.96
L_1/FA_1	29.69	0.0612	0.0543	0.0113	3.96
L_2/FA_1	47.89	0.0913	0.0810	0.0162	4.06

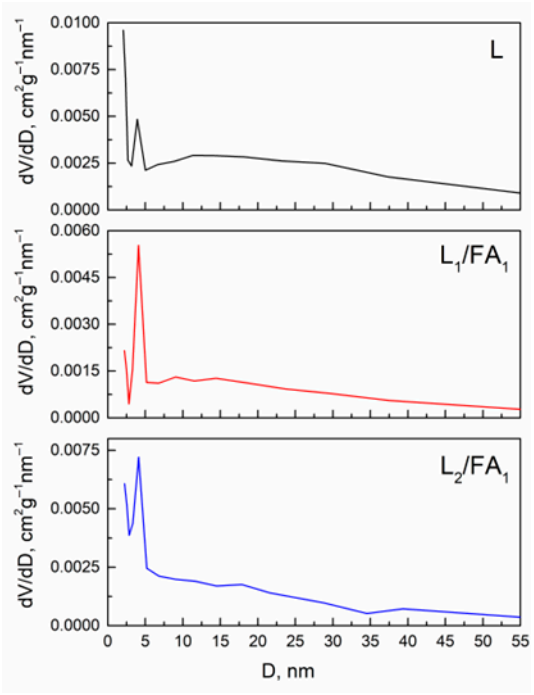


Figure 2. Pore size distribution of the examined samples.

Structural analysis based on the XRD patterns (Figure 3) indicates the presence of both amorphous and crystalline phases in all examined samples. The broad halo observed in the 2θ range of 20–40° in the XRD pattern of sample L is characteristic of a disordered carbon structure. In the hybrid samples, a similar broad feature is also present in this region, which, in addition to the disordered carbon, can be attributed to the amorphous aluminosilicate phase formed during the activation process. For all samples, a distinct diffraction peak at 14.6° can be attributed to the crystalline structure of cellulose I, while peaks at 24.4° and 43° indicate the formation of a layered graphite-type structure [36–38]. The intensity of these peaks is higher for L_2/FA_1 than for L_1/FA_1 due to the higher amount of flax fibers used for sample preparation. The presence of a crystalline cellulose peak and the low peak at 43° indicate partial transformation of flax into carbonaceous material. In samples consisting of a mixture of flax and fly ash, peaks from quartz are observed at 26.7°, 36.4°, 50°, 60°, and 68° [39,40]. The formation of sodium silicate is confirmed by the presence of a peak at 20.9°, while peaks at 27.7° and 34.5° indicate the presence of sodium aluminum silicate [41]. Additionally, a peak at 39.5° in the XRD spectra of hybrid adsorbents corresponds to the crystalline phases of mullite, characteristic of the fly ash used (Figure S1a) [42].

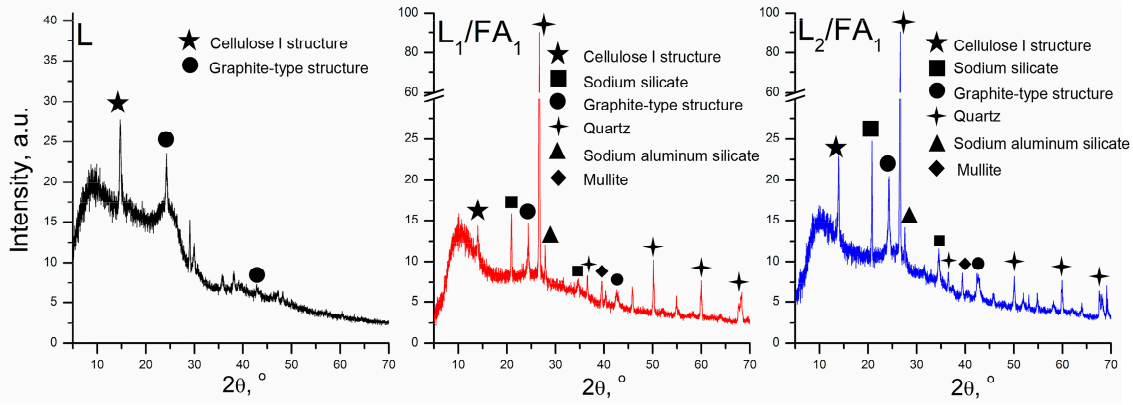


Figure 3. XRD spectra of the synthesized samples.

The thermal behavior and oxidation stability of the samples (L, L_1/FA_1, and L_2/FA_1) were evaluated by thermogravimetric and derivative thermogravimetric analyses under air at up to 800 °C (Figure 4a). The TGA curves (Figure 4a) reveal that all samples exhibit a small initial mass loss below 120 °C, which can be attributed to the removal of physically adsorbed moisture. This process is recorded as small peaks around 120 °C on the DTG curves for all samples (Figure 4b). For the L sample, a significant mass loss (from 97 to 10%) was observed in the temperature range from 350 to 530 °C, indicating rapid oxidation of the carbonaceous structure [43], and cellulose remained in the structure of the obtained sample (Figure 3). Two partially overlapping sharp and intense DTG peaks (Figure 4b) suggest that multiple oxidation processes may occur simultaneously. On the other hand, the hybrid samples, L_1/FA_1 and L_2/FA_1, show a gradual mass decrease in the temperature range from 120 to 400 °C. This mass loss can be associated with the decomposition of residual organic components and the onset of oxidation processes of the carbonaceous matrix. The main oxidation and mass loss of the hybrid samples occur in the temperature range of 400–540 °C. The L_1/FA_1 and L_2/FA_1 samples exhibit significantly lower and broader DTG peaks, with maxima shifted slightly toward higher temperatures. This indicates a slower and less intense oxidation process. The reduced peak intensity and peak broadening suggest that the addition of fly ash and its activation with NaOH lead to a more heterogeneous structure and limit oxygen diffusion to reactive sites. Furthermore, the hybrid samples retain a significantly higher residual mass (78% for L_1/FA_1 and 82% for L_2/FA_1 at 800 °C) due to the presence of an inorganic fly ash fraction, which remains thermally stable under oxidative conditions. The mass loss at 800 °C indicates that, regardless of the mass ratio of flax and fly ash in the initial reaction mixture, the hybrid materials contain approximately 80% of the inorganic component derived from fly ash and only about 20% of carbonized flax, due to the significant mass loss occurring during the carbonization of flax. The lower mass loss and better stability observed for sample L_2/FA_1 may be attributed to its specific morphology, i.e., surface coverage by the spherical particles originating from fly ash (Figure 1c) that may act as a thermal barrier and influence oxidation.

The functional groups of all samples (Figure 5) were determined by Fourier transform infrared spectroscopy. In the spectra obtained for sample L, the broad bands in the range of 3422–3334 cm^{-1} correspond to the OH band, more precisely to the vibrations of intramolecular hydrogen bonds of hydroxyl groups in cellulose [36,44]. The peaks detected at 1610 cm^{-1}, 1435 cm^{-1}, and 753 cm^{-1} associated with the –C=C bending vibrations of the aromatic skeleton and –C–H bonds indicate that the lignin structure remained [45] at the flax pyrolysis temperature of 500 °C. Partial degradation of the cellulose matrix in raw flax during pyrolysis and activation is indicated by a decrease in the intensity of the peaks at 2918 cm^{-1} and 2853 cm^{-1}, corresponding to asymmetric/symmetric C–H vibrations in

methylene groups. Peaks at 1318, 1158, and 1030 cm^{-1} can be assigned to C–O, C–O–C, and O–H bending vibrations of residual cellulose, confirming the incomplete decomposition of polysaccharides. The presence of a band around 890 cm^{-1} further supports the persistence of β-glycosidic linkages, indicating partial carbonization. In addition, the peak at 1730 cm^{-1} from the C=O stretching vibrations of the carboxyl/ester groups of hemicelluloses is absent [30]. These findings confirm that flax fibers are not completely converted into carbonized material. In the spectra of flax samples mixed with fly ash, additional characteristic peaks can be observed. The low-intensity peaks observed at 1635 cm^{-1} can be attributed to H–O–H bending vibrations in adsorbed water. The effect of temperature and alkali activation is visible in the spectra as a shift of the band at 1090 cm^{-1} (FTIR spectra of initial raw FA are given in Figure S1) to lower wavenumbers, i.e., to around 980 cm^{-1} in the L_1/FA_1 and L_2/FA_1 spectra [46]. This band, as well as the peak at 425 cm^{-1}, corresponds to vibrations of the Al–O and Si–O bonds [44] and indicates the formation of a polymer gel network structure (Si–O–Si or Si–O–Al) as a result of the applied modification that can contribute to enhanced adsorption performance.

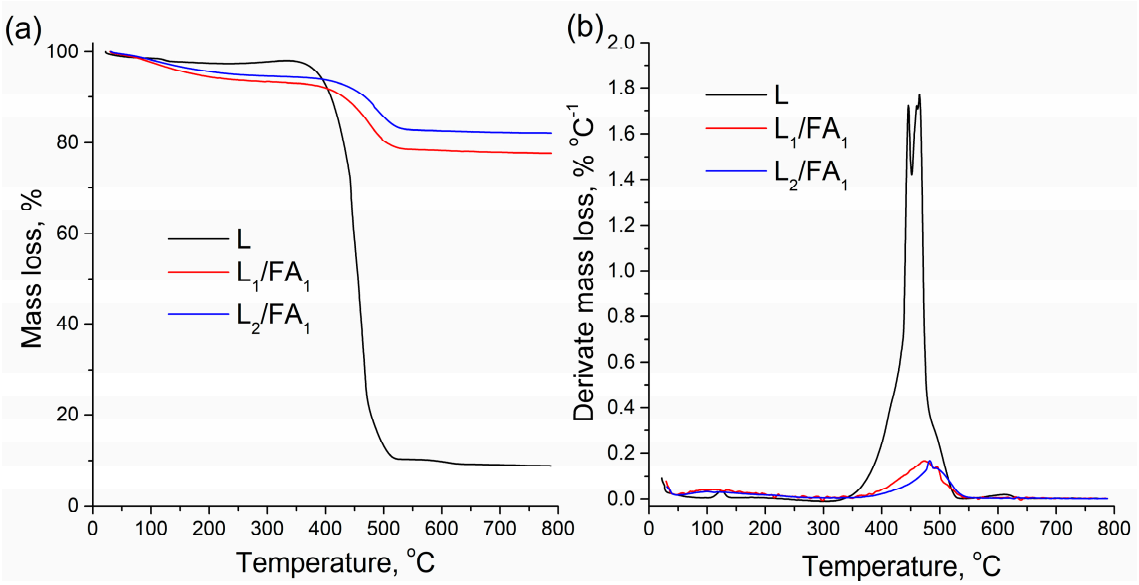


Figure 4. TGA (**a**) and DTG (**b**) curves of the examined samples.

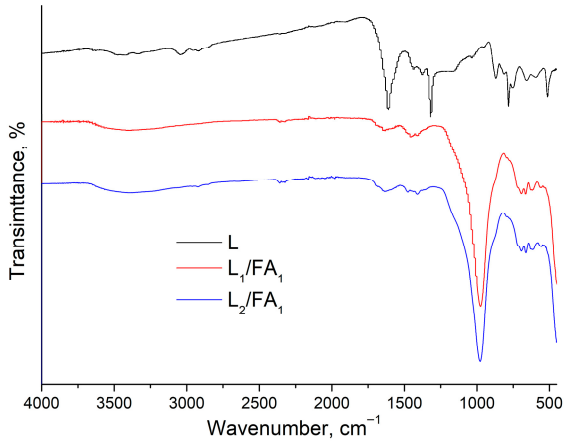


Figure 5. FTIR spectra of the synthesized samples.

The effect of fly ash content in the starting mixture used for material synthesis on the surface charge properties of the obtained samples was evaluated by determining the point

of zero charge (pH_{PZC}) (Figure 6). An increase in fly ash content led to a progressive rise in pH_{PZC} values, from 6.38 for the fly ash-free sample (L), to 9.78 for sample L_2/FA_1, and up to 11.2 for sample L_1/FA_1 containing the highest proportion of fly ash.

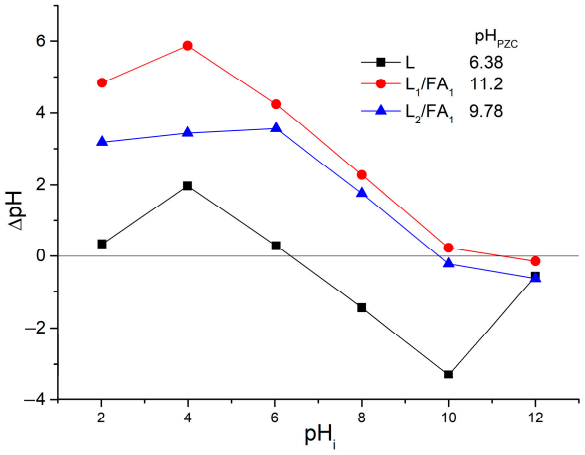


Figure 6. Point of zero charge of the examined samples.

3.2. Adsorption Experiments

The adsorption efficiency of the obtained hybrid adsorbents for the removal of rare earth elements from water was investigated and compared to the adsorption efficiencies of fly ash and carbonized flax fibers. Based on the results (Figure 7), all examined samples showed the highest adsorption efficiency for the scandium ion, while the adsorbent L_1/FA_1 also showed increased adsorption efficiencies for yttrium and gadolinium ions. Carbonized flax fibers showed the lowest adsorption efficiency, followed by unmodified fly ash, while the hybrid adsorbents exhibited higher adsorption efficiencies. Despite the highest specific surface area (Table 1) and the formation of a carbonaceous structure during carbonization (Figure 3), the L sample showed a relatively low adsorption efficiency (Figure 7). Unmodified fly ash exhibits slightly better adsorption properties than carbonized flax fibers due to its distinct mineral structure (Figure S1a) that can contribute to adsorption through ion exchange and surface interactions. A significant improvement in adsorption efficiency was observed for the hybrid adsorbents. This improvement can be attributed to the alkaline activation of fly ash in the presence of NaOH. As reported in the literature [47,48], the properties of geopolymers strongly depend on the concentration of NaOH used for activation. Higher NaOH concentrations (e.g., ~12 M) are typically associated with the formation of mechanically robust structures, while moderate concentrations (e.g., ~6 M) are more suitable for generating reactive aluminosilicate surfaces with enhanced adsorption properties. In this study, a 5 M NaOH solution was selected as a moderate activation condition based on literature considerations, and the NaOH concentration was not optimized but rather fixed in order to enable a consistent comparison between materials with different compositions. The observed improvement in adsorption performance of the hybrid adsorbents compared to unactivated fly ash (Figure 7) is therefore attributed primarily to the synergistic interaction between the carbonaceous and inorganic phases, rather than to variations in synthesis conditions. The presence of fly ash in the composite material plays an important role in enhancing the adsorption properties, as sample L_1/FA_1 with a higher fly ash content demonstrated better adsorption performance than L_2/FA_1. Higher adsorption efficiencies of hybrid adsorbents that exhibited a lower specific surface area than sample L indicate that their adsorption behavior is not governed solely by specific surface area. Sample L_1/FA_1 is characterized by a more basic surface (as indicated by its higher pH_{PZC} value), suggesting that adsorption is also governed by surface chemical

composition, i.e., the presence and nature of functional groups. Additionally, XRD analysis (Figure 3) revealed a slightly higher crystallinity of the L_2/FA_1 surface, which can have a negative effect on the adsorption properties. Due to the enhanced adsorption properties, the hybrid adsorbents were chosen for the optimization of REE adsorption parameters.

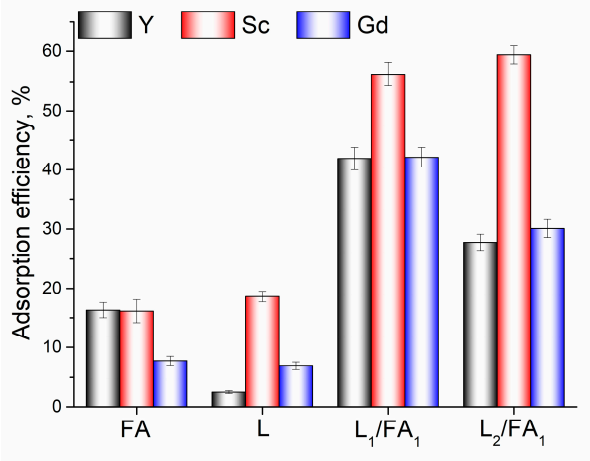


Figure 7. Adsorption efficiencies of carbonized flax fibers and hybrid adsorbents for REE removal from water.

The initial pH of an aqueous solution containing REEs is a key parameter influencing the adsorption process. Variations in pH can alter the ionization state of functional groups on the adsorbent surface, thereby affecting the surface charge and its interaction with metal ions. In addition, pH influences the speciation and stability of metal ions present in the solution. To prevent precipitation of REE hydroxides, the influence of pH on adsorption was examined by varying pH from 2 to 4. According to the speciation (Figure S2), in this pH range, the trivalent rare earth metal cations prevail. The effect of the initial pH on the adsorption efficiencies of the hybrid adsorbents is presented in Figure 8. The adsorption behavior of Y, Sc, and Gd onto hybrid adsorbents was strongly dependent on the pH of the system. The L1/FA1 sample exhibited increased adsorption efficiency up to pH 3.5, showing that this value is optimal for REEs adsorption. For sample L_2/FA_1, the highest adsorption efficiency was achieved at pH 3 for all selected analytes, and that pH value was chosen for the following adsorption experiments on this sample. Considering that the adsorption experiments were conducted at pH values lower than the corresponding pH_{PZC} values, the adsorbent surfaces are expected to be positively charged due to the protonation of surface functional groups. Under such conditions, electrostatic attraction between the surface and cationic species would be unfavorable, suggesting that adsorption is not governed by electrostatic interactions. Nevertheless, the observed high adsorption efficiencies indicate that alternative mechanisms are involved. Adsorption of rare earth ions, such as Sc^{3+}, Gd^{3+}, and Y^{3+}, is largely determined by their pronounced Lewis acid nature and high positive charge, which indicates a more significant role of chemical interactions in relation to purely physical adsorption. According to the HSAB (hard and soft acids and bases) theory, these ions are classified as "hard" Lewis acids, with a pronounced preference for oxygen-containing electron pair donors [49]. It is therefore proposed that adsorption predominantly occurs via defect sites and inner-sphere complexation. Among the investigated ions, Sc^{3+} exhibits the highest affinity for the adsorbent, which can be attributed to a smaller ionic radius (~0.75 Å). In contrast, the lower adsorption efficiency obtained for Y^{3+} and Gd^{3+} can be the consequence of their larger ionic radii (~0.90 Å and ~0.94 Å, respectively) and more pronounced hydration shells. Even under acidic conditions,

where the adsorbent surface is positively charged, the presence of defect sites and strong Lewis acid–base interactions enables significant adsorption, particularly in the case of Sc^{3+}.

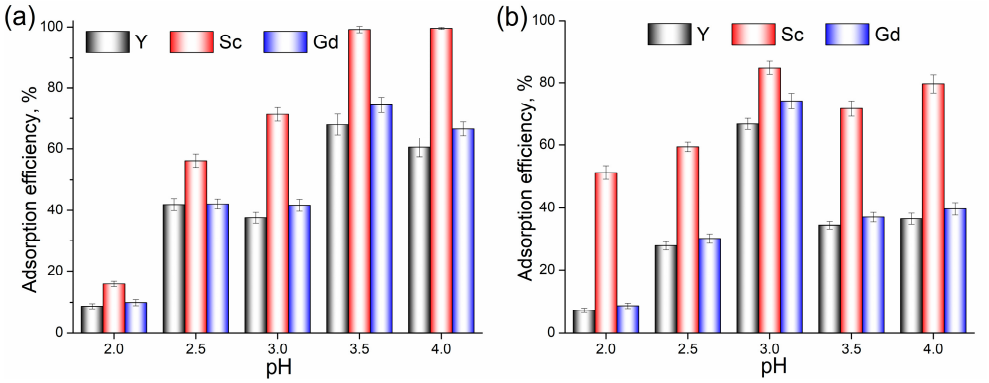


Figure 8. The influence of the initial pH value of the REE solution on the adsorption efficiency of (**a**) L_1/FA_1 and (**b**) L_2/FA_1.

The effect of contact time on the adsorption efficiency is presented in Figure 9. Investigating the effect of contact time provides insight into the adsorption kinetics and identifies the time required to reach maximum adsorption capacity. The adsorption capacities of the examined samples increase with adsorption time, approaching equilibrium after 48 h. At the initial stage, the adsorption was relatively fast due to the abundance of available active sites on the adsorbent surface and the concentration gradient, and it slowed down after the first three hours. Both samples exhibited the highest adsorption capacities for the adsorption of scandium. For the trivalent rare earth ions, dominant in the solution (Figure S2), differences in hydrated radii can affect their adsorption behavior on the examined hybrid adsorbents. Scandium ions, with smaller hydrated radii, more easily diffuse through the pore structure of the adsorbent and interact with surface functional groups, leading to more efficient adsorption.

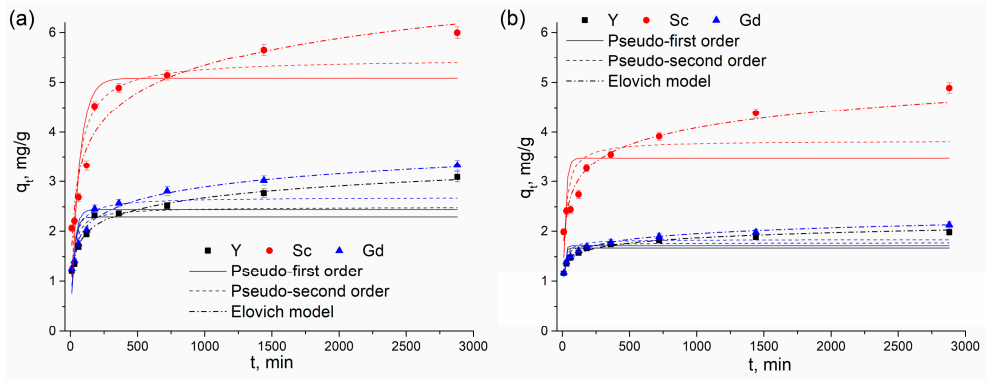


Figure 9. The influence of contact time on adsorption onto (**a**) L_1/FA_1 and (**b**) L_2/FA_1, and fitting of the experimental results with kinetic models.

Experimental kinetic data were analyzed using the Elovich, pseudo-first-order, and pseudo-second-order models (Figure 9), together with the intraparticle diffusion model (Figure S3). The corresponding kinetic parameters are summarized in Tables 2 and 3. Based on the correlation coefficients (R^2) and the comparison between experimentally determined and model-predicted adsorption capacities, the pseudo-second-order model provides a better description of the adsorption kinetics than the pseudo-first-order model. However, the highest R^2 values were obtained for the Elovich model, suggesting that the adsorption of REE ions onto the hybrid adsorbents is most adequately described by the Elovich

kinetic model. The results further indicate that varying the ratios of flax fibers and fly ash used in the preparation of the hybrid adsorbents significantly influences the adsorption kinetics. Specifically, differences are observed in the initial adsorption rate, reflected by the Elovich parameter α, as well as in the surface coverage behavior, represented by parameter β. The higher value of the Elovich coefficient α (Table 2) obtained for sample L_2/FA_1 indicates a faster initial uptake of REE ions and suggests a more pronounced contribution of chemisorption to the overall adsorption mechanism. In addition, the higher β value obtained for this sample implies a greater degree of surface coverage during the adsorption process. The enhanced adsorption performance observed for sample L_2/FA_1 is most likely associated with its higher specific surface area available for adsorption. These structural characteristics facilitate faster adsorption kinetics and increased accessibility of active sites. Furthermore, the higher α value relative to β suggests that the adsorption of REE ions onto L_2/FA_1 proceeds efficiently, particularly during the initial stages of the process.

Table 2. Kinetic parameters for the adsorption of REE ions onto L_1/FA_1 and L_2/FA_1.

	Sample	**L_1/FA_1**			**L_2/FA_1**		
	REE	**Y**	**Sc**	**Gd**	**Y**	**Sc**	**Gd**
PSI *	$q_{e,cal}$, mg g^{-1}	2.30	5.08	2.44	1.67	3.48	1.72
	k_1, min^{-1}	0.0400	0.0164	0.0376	0.1076	0.0560	0.1034
	R^2	0.54861	0.68718	0.50011	0.54111	0.35984	0.50754
PSII *	$q_{e,cal}$, mg g^{-1}	2.49	5.47	2.69	1.77	3.83	1.84
	k_2, g mg^{-1} min^{-1}	0.0231	0.0045	0.0194	0.0883	0.0164	0.0786
	R^2	0.78488	0.82085	0.75198	0.82019	0.64053	0.77991
$q_{e,exp}$, mg g^{-1}		2.77	5.66	3.02	1.89	4.38	1.98
Elovich kinetic	α, mg g^{-1} min^{-1}	0.9641	0.7040	0.8192	52.15	1.958	24.02
	β, g mg^{-1}	2.972	1.273	2.657	6.837	2.026	6.089
	R^2	0.96685	0.92864	0.96199	0.98616	0.95762	0.99576

* PSI-pseudo-first kinetic model, PSII-pseudo-second kinetic model.

Table 3. Intraparticle diffusion parameters for the adsorption of REE ions onto L_1/FA_1 and L_2/FA_1.

Sample	**REE**	**$k_{id,1}$, mg/(g·$min^{1/2}$)**	**C_1, mg/g**	**R^2**	**$k_{id,2}$, mg/(g·$min^{1/2}$)**	**C_2, mg/g**	**R^2**
L_1/FA_1	Y	0.109	0.817	0.97903	0.019	2.075	0.99721
	Sc	0.235	1.047	0.89420	0.037	4.087	0.93952
	Gd	0.115	0.846	0.97361	0.022	2.178	0.99704
L_2/FA_1	Y	0.046	1.072	0.93476	0.008	1.570	0.97726
	Sc	0.110	1.672	0.91121	0.041	2.745	0.98360
	Gd	0.048	1.086	0.92736	0.011	1.558	0.99259

The intraparticle diffusion model was applied to reveal the influence of diffusion on the adsorption process. The obtained multilinear q_t vs $t^{1/2}$ plots (Figure S3) do not pass through the origin, indicating that intraparticle diffusion is not the rate-controlling process of REE adsorption onto hybrid adsorbents. Although intraparticle diffusion is not the sole rate-controlling step of the adsorption process, the experimental results indicate that the diffusion of REE ions still contributes to the overall adsorption kinetics. An initial rapid

adsorption stage is observed, which is facilitated by efficient mixing of the system. As the adsorption proceeds, the surface coverage gradually increases, and the adsorption slows down (values of $k_{id,1} > k_{id,2}$ for adsorption of the examined REEs onto both samples) due to the slower diffusion of REE ions from the bulk solution toward the adsorbent surface, which is particularly evident for the adsorption of Sc^{3+} (Table 3). The intraparticle diffusion model parameters C_1 and C_2, which reflect the thickness of the boundary layer and the contribution of film diffusion, were highest for Sc^{3+} adsorption, confirming the stronger influence of external mass transfer resistance in this case.

The influence of initial concentration on REE adsorption is given in Figure 10. The adsorption capacities of the hybrid adsorbents increased with the initial concentration of REEs in solution, reaching a plateau at initial concentrations of 75–100 mg/dm^3, which indicates surface saturation.

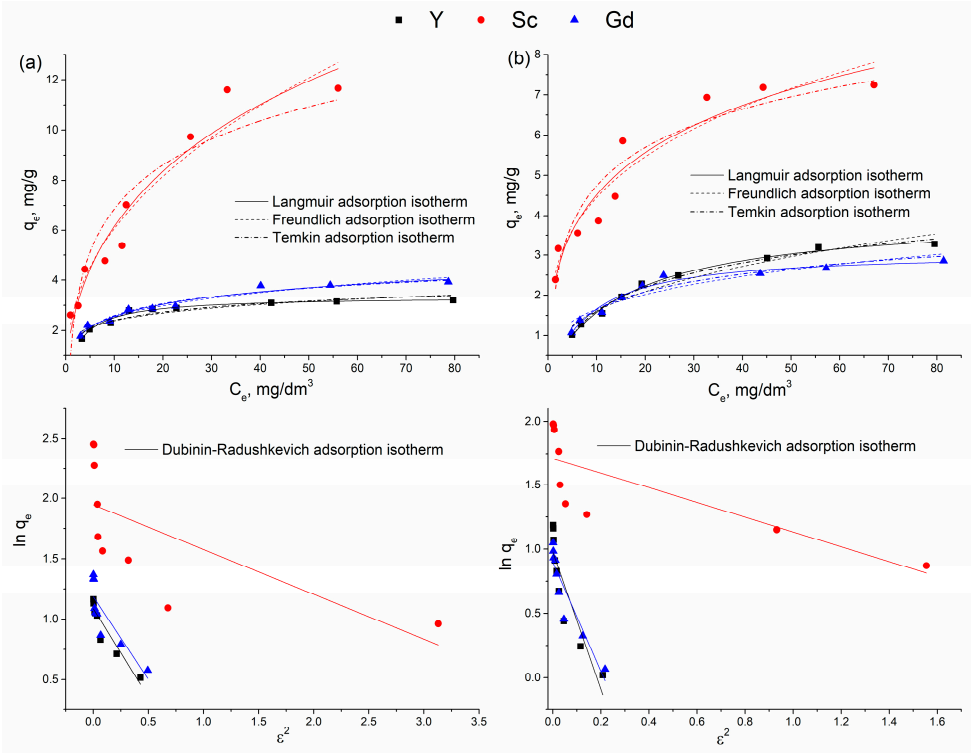


Figure 10. The influence of initial concentration on REE adsorption onto (**a**) L_1/FA_1 and (**b**) L_2/FA_1, and the fitting of the experimental results with isotherm models.

The equilibrium adsorption data were analyzed by isotherm models, and the obtained parameters are summarized in Table 4. According to the correlation coefficients, the equilibrium data for adsorption of Y^{3+} and Gd^{3+} on both hybrid adsorbents are better described by the Langmuir isotherm model, while adsorption of Sc^{3+} better fits the Freundlich model. According to the Freundlich adsorption isotherm model, smaller values of the $1/n$ parameter are associated with greater heterogeneity of the adsorbent surface and a wider distribution of adsorption site energies [50]. The values of $1/n$ obtained for both adsorbents fall within the range $0 < 1/n < 1$, indicating a heterogeneous surface of the adsorbents, a strong affinity toward the adsorbate, and a favorable adsorption process under the investigated conditions. The lower values of $1/n$ obtained for the adsorption of Y^{3+} and Gd^{3+} onto L_1/FA_1 suggest a higher degree of surface heterogeneity of this sample compared to L_2/FA_1. The higher affinity of Y^{3+} and Gd^{3+} toward the sample L_1/FA_1 is supported by the elevated values of the Temkin constant A.

Table 4. Isotherm parameters for the adsorption of REEs onto L_1/FA_1 and L_2/FA_1.

Material	REE	Langmuir Isotherm			Freundlich Isotherm		
		q_0, mg g^{-1}	b	R^2	K_f, mg g^{-1} (mg dm^{-3})$^{-1/n}$	$1/n$	R^2
L_1/FA_1	Y	3.341	0.3035	0.97128	1.614	0.171	0.84890
	Sc	32.32	0.0640	0.92476	2.271	0.427	0.93135
	Gd	7.179	0.2193	0.95627	1.486	0.233	0.95554
L_2/FA_1	Y	4.027	0.0699	0.99105	0.674	0.378	0.95050
	Sc	18.28	0.1265	0.89907	2.259	0.295	0.90913
	Gd	3.050	0.0929	0.96383	0.856	0.287	0.88115
		Temkin Isotherm			Dubinin–Radushkevich Isotherm			
		A, dm^3 g^{-1}	b_t, kJ mol^{-1}	R^2	q_m, mg g^{-1}	β, mol^2 J^{-2}	E kJ mol^{-1}	R^2
L_1/FA_1	Y	15.7	5.213	0.90025	2.963	1.461	0.585	0.87009
	Sc	1.52	0.982	0.85794	7.002	0.370	1.162	0.38626
	Gd	4.61	3.657	0.95965	3.269	1.366	0.605	0.67928
L_2/FA_1	Y	0.64	2.868	0.98697	2.657	5.333	0.306	0.79077
	Sc	3.19	1.808	0.88854	5.521	0.576	0.932	0.57880
	Gd	1.35	3.916	0.93752	2.453	4.235	0.344	0.84077

The highest Langmuir maximum adsorption capacities were obtained for the adsorption of Sc^{3+} onto both hybrid adsorbents, which are consistent with the values of the Freundlich constant K_f and the Dubinin–Radushkevich parameter q_m. Notably, the q_m values derived from the Dubinin–Radushkevich model are in better agreement with the experimentally determined adsorption capacities than the Langmuir q_0 values. Furthermore, the relatively low values of the Temkin constant b_t (Table 4) suggest that the adsorption of REE ions onto the surface of the hybrid adsorbents is predominantly governed by physical interactions. This interpretation is consistent with the Dubinin–Radushkevich mean adsorption energy values, which are below 2 kJ/mol, confirming the physisorption mechanism.

To assess the thermodynamic aspects of the process, adsorption experiments were carried out at 25, 35, and 45 °C, and the resulting data were used to evaluate the relevant thermodynamic parameters governing REE ion uptake onto hybrid adsorbents. The obtained values of thermodynamic parameters (Table 5) indicate differences in the adsorption behavior of the examined hybrid adsorbents. Adsorption of REE ions onto L_1/FA_1 is endothermic, and adsorption onto L_2/FA_1 is an exothermic process. The Gibbs free energy values are negative across the entire temperature range only for the adsorption of Sc^{3+} on both adsorbents, indicating a spontaneous process. For the adsorption onto L_1/FA_1, the decrease in ΔG with increasing temperature indicates that adsorption of Sc becomes more favorable at elevated temperatures, and adsorption of gadolinium tends toward spontaneity as temperature increases (ΔG < 0 at 45 °C). The positive ΔS values obtained for all three ions imply increased randomness at the solid–solution interface due to dehydration of hydrated ions and subsequent interaction with active sites. Conversely, for adsorption of Y^{3+} and Gd^{3+} on L_2/FA_1, positive ΔG values increase with temperature, indicating that their adsorption becomes less favorable at higher temperatures, which is consistent with the exothermic nature of the process. The negative ΔS values obtained for the L_2/FA_1 sample suggest decreased randomness at the interface, which may be attributed to a more ordered arrangement of ions on the adsorbent surface.

Table 5. Thermodynamic parameters (ΔG, ΔH, ΔS) for REE adsorption onto hybrid adsorbents.

Material	REE	ΔH, kJ mol^{-1}	ΔS, J mol^{-1} K^{-1}	ΔG, kJ mol^{-1}		
				298.15 K	308.15 K	318.15 K
L_1/FA_1	Y	50.80	0.157	3.74	2.16	0.58
	Sc	183.03	0.629	−4.39	−10.67	−16.96
	Gd	57.55	0.181	3.58	1.77	−0.041
L_2/FA_1	Y	−17.41	−0.068	2.92	3.59	4.28
	Sc	−31.86	−0.077	−8.74	−7.97	−7.19
	Gd	−22.08	−0.083	2.57	3.39	4.22

Generally, the obtained ΔG and ΔH values indicate contrasting thermodynamic behavior between L_1/FA_1 and L_2/FA_1, suggesting different mechanisms governing REE adsorption onto these materials. The relatively high positive ΔH values observed for L_1/FA_1 point to an endothermic process involving a combination of physisorption and chemisorption. In particular, the markedly high ΔH value for Sc^{3+} (183.03 kJ/mol) implies strong interactions with the adsorbent surface, consistent with chemisorption or inner-sphere complexation. In contrast, the thermodynamic parameters for L_2/FA_1 indicate an exothermic process with lower ΔH values, suggesting that adsorption is predominantly governed by physisorption, which is in agreement with the isotherm analysis. However, the physisorption mechanism obtained from model fitting is not fully consistent with the surface characterization results. Specifically, considering the pH conditions below the pH_{PZC}, the adsorbent surface is positively charged, leading to electrostatic repulsion with the positively charged REE ions in solution. This indicates that additional mechanisms must contribute to the overall adsorption process. As previously discussed, even under acidic conditions, the presence of defect sites and strong Lewis acid–base interactions enables significant adsorption, particularly for Sc^{3+}. Owing to its small ionic radius and high charge density, Sc^{3+} exhibits a strong tendency to coordinate with oxygen-containing functional groups on the adsorbent surface, favoring the formation of stable inner-sphere complexes [51,52]. In contrast, Gd^{3+} and Y^{3+} ions, although also classified as hard Lewis acids, are characterized by larger ionic radii and greater coordination flexibility. Their adsorption is therefore less pronounced and likely involves a combination of mechanisms, including weaker surface complexation and ion exchange [53,54].

To compare the adsorption properties of the obtained adsorbents with the adsorbents used for rare earth adsorption, the literature data are summarized in Table 6. According to the literature, for the adsorption of selected REEs, variously modified fly ash, carbon nanotubes, and silica-based adsorbents were used, whereas few investigations have examined the application of carbonaceous adsorbents derived from waste biomass. As can be seen from Table 6, the adsorption capacities of the obtained hybrid adsorbents are lower. Nevertheless, the production of these materials involves the utilization of two abundant waste streams, a simple synthesis procedure, low consumption of non-toxic chemicals, and their application for the removal of REEs, which has not been extensively investigated. Furthermore, the adsorption performance of hybrid adsorbents obtained in this work is strongly influenced by material composition and structural features. As the synthesis parameters were not optimized in this study, further improvements in adsorption efficiency are expected through systematic optimization of synthesis conditions, which will be the subject of future research.

Table 6. Comparison of REE adsorption onto different materials.

Adsorbent	REE	Initial Conc. (mg/dm^3)	Mass of Adsorbent (g)	Solution Volume (cm^3)	Chemical/Thermal Modification	Adsorption Capacity (mg/g)	Ref.
alkali activated fly ash (with/without wood ash)	Gd, Y, Sc	10	0.05	20	alkali activation	5.090 for Gd, 5.010 for Y, 4.020 for Sc	[40]
geopolymer from coal fly ash	La, Ce, Nd, Sm, Gd, Dy, Er, Y	1	0.5003 0.5200	50	geopolymerization	-	[15]
PAN/APTES silica and chitosan particles	La, Sc, Y	25	0.01	10	polymer functionalization	120.7 for La, 175.22 for Sc, 158.8 for Y	[54]
PAN grafted SWNT(MWNT)-APTES nanosilica	La, Sc, Y	5	0.01	10	organic–inorganic hybrid modification	80.68 (103.2) for La, 12.68 (32.92) for Sc, 48.34 (68.78) for Y	[55]
Cellulose–silica nanocomposite	La, Sc, Eu	25	0.03	10	chemical functionalization and silica hybridization	29.48 for La, 23.76 for Sc, 24.27 for Eu	[56]
glycine-modified activated carbon from navel orange peel	Gd	50	0.03	50	glycine-assisted carbonization 500 °C for 1 h in a nitrogen atmosphere	31.19	[57]
pine wood sawdust	Sc, Nd	20	1–10 g/L	-	350 and 550 °C in a nitrogen atmosphere	1.05–7.58 for Sc	[58]
waste flax fibers and fly ash	Y, Sc, Gd	7.5–100	0.05	20	alkali activation 500 °C in a nitrogen atmosphere	3.27 for Y, 11.7 for Sc, 3.93 for Gd	this study

4. Conclusions

New hybrid adsorbents were successfully synthesized by thermal treatment of waste flax fibers and fly ash in the presence of sodium hydroxide. The presence of cellulose and lignin residues in XRD and FTIR spectra indicates incomplete conversion of flax fibers into carbon material. At the same time, it was shown that the specific surface area and porosity of the hybrid adsorbents originate mainly from the pyrolysis of flax fibers, while the increase in the number of active sites for adsorption is attributed to the formation of an aluminosilicate network through the activation of fly ash. Although the increase in the fly ash content led to a decrease in the specific surface area, the hybrid materials exhibited improved adsorption characteristics, significantly outperforming the individual components. Applied theoretical models suggest a physisorption-governed process; however, surface characterization and experimental conditions demonstrate that the adsorption of Sc^{3+} primarily occurs through chemisorption via inner-sphere complexation. Although the obtained adsorption capacities are moderate, the developed hybrid materials demonstrate the feasibility of integrating two abundant waste streams into functional, cost-effective, and sustainable adsorbents for the removal of rare earth elements from aqueous systems. Future studies will focus on the systematic investigation of synthesis parameters to further enhance the adsorption performance of these materials.

Supplementary Materials: The following supporting information can be downloaded at: https://www.mdpi.com/article/10.3390/separations13050138/s1, Figure S1: (a) XRD and (b) FTIR spectra of fly ash; Figure S2: Speciation of REE ions in aqueous solution; Figure S3: Intraparticle diffusion plots for samples (a) L_1/FA_1 and (b) L_2/FA_1; Table S1: Equations for kinetic and isotherm models and thermodynamics. References [59–66] are cited in the supplementary materials.

Author Contributions: Conceptualization, M.V., K.T. and T.R.; methodology, M.V., A.K. and M.M.; software, I.J.-Č.; formal analysis, I.J.-Č. and T.R.; investigation, T.R., I.J.-Č., M.M., A.K. and M.S.; data

curation, T.R., M.M., A.K. and M.S.; writing—original draft preparation, T.R. and M.S.; writing—review and editing, M.V., K.T. and M.M.; supervision, M.V. and K.T. All authors have read and agreed to the published version of the manuscript.

Funding: This work was supported by the Ministry of Science, Technological Development and Innovation of the Republic of Serbia (Contract No. 451-03-34/2026-03/200135, 451-03-33/2026-03/200287 and 451-03-33/2026-03/200017).

Institutional Review Board Statement: Not applicable.

Informed Consent Statement: Not applicable.

Data Availability Statement: The data presented in this study are available on request from the corresponding author.

Conflicts of Interest: The author Tijana Radojičić is an employee of MDPI; however, she did not work for the journal *Separations* at the time of submission and publication. Author Marina Maletić is employed by Innovation Centre, Faculty of Technology and Metallurgy. All authors declare that the research was conducted in the absence of any commercial or financial relationships that could be construed as a potential conflict of interest.

References

1. Lakić, M.; Breijaert, T.C.; Daniel, G.; Svensson, F.G.; Kessler, V.G.; Seisenbaeva, G.A. Uptake and separation of rare earth elements and late transition metal cations by nanoadsorbent grafted with diamino ligands. *Sep. Purif. Technol.* **2023**, *323*, 124487. [CrossRef]
2. Hu, Y.; Florek, J.; Larivière, D.; Fontaine, F.-G.; Kleitz, F. Recent Advances in the Separation of Rare Earth Elements Using Mesoporous Hybrid Materials. *Chem. Rec.* **2018**, *18*, 1261–1276. [CrossRef]
3. Yıldız, T.D. Opportunities for the Recovery of Rare Earth Elements from Mining Tailings and Urban Mining. In *Trash or Treasure*; Singh, P., Borthakur, A., Eds.; Springer: Cham, Switzerland, 2024; pp. 183–205. [CrossRef]
4. Ambaye, T.G.; Vaccari, M.; Castro, F.D.; Prasad, S.; Rtimi, S. Emerging technologies for the recovery of rare earth elements (REEs) from the end-of-life electronic wastes: A review on progress, challenges, and perspectives. *Environ. Sci. Pollut. Res.* **2020**, *27*, 36052–36074. [CrossRef]
5. Dardona, M.; Mohanty, S.K.; Allen, M.J.; Dittrich, T.M. From ash to oxides: Recovery of rare-earth elements as a step to-wards valorization of coal fly ash waste. *Sep. Purif. Technol.* **2023**, *314*, 123532. [CrossRef]
6. Sandeep, P.; Maity, S.; Mishra, S.; Chaudhary, D.K.; Dusane, C.B.; Pillai, A.S.; Kumar, A.V. Estimation of rare earth elements in Indian coal fly ashes for recovery feasibility as a secondary source. *J. Hazard. Mater. Adv.* **2023**, *10*, 100257. [CrossRef]
7. Mkilima, T. Nature-Based Hybrid Adsorbents for Emerging Contaminant Removal: Integrating Low-Cost Bioresources in the Water–Energy–Food Nexus. *Earth Environ. Sustain.* **2025**, *1*, 276–302. [CrossRef]
8. Kalyankar, S.S.; Antanitta, S.V.; Dixit, F.; Zimmermann, K.; Kandasubramanian, B. Composite Materials for Adsorption of Rare Earth Metal Ions. *Water Air Soil Pollut.* **2025**, *235*, 661. [CrossRef]
9. Elwakeel, K.Z.; Mohammad, R.M.; Alghamdi, H.M.; Elgarahy, A.M. Hybrid adsorbents for pollutants removal: A comprehensive review of chitosan, glycidyl methacrylate and their composites. *J. Mol. Liq.* **2025**, *426*, 127262. [CrossRef]
10. Huang, M.-M.; Tan, J.; Xia, L.-Y.; Han, K.; Cai, H.-Y.; Ma, X.; Wang, S. A Comprehensive Review of Adsorbents for Rare Earth Separation: Design, Synthesis, Adsorption Performance, and Mechanisms. *Rare Met.* **2026**, *45*, 70056. [CrossRef]
11. Vukčević, M.; Maletić, M.; Pejić, B.; Karić, N.; Trivunac, K.; Perić Grujić, A. Waste hemp and flax fibers and cotton and cotton/polyester yarns for removal of methylene blue from wastewater: Comparative study of adsorption properties. *J. Serb. Chem. Soc.* **2023**, *88*, 669–683. [CrossRef]
12. Liu, Y.; Yan, C.; Zhang, Z.; Wang, H.; Zhou, S.; Zhou, W. A comparative study on fly ash, geopolymer and faujasite block for Pb removal from aqueous solution. *Fuel* **2016**, *185*, 181–189. [CrossRef]
13. Eteba, A.; Bassyouni, M.; Saleh, M. Modified coal fly ash for textile dye removal from industrial wastewater. *Energy Environ.* **2022**, *35*, 1004–1030. [CrossRef]
14. Gupta, P.; Nagpal, G.; Gupta, N. Fly ash-based geopolymers: An emerging sustainable solution for heavy metal remediation from aqueous medium. *Beni-Suef Univ. J. Basic Appl. Sci.* **2021**, *10*, 89. [CrossRef]
15. Fiket, Ž.; Galović, A.; Medunić, G.; Turk, M.F.; Ivanić, M.; Dolenec, M.; Biljan, I.; Šoster, A.; Kniewald, G. Adsorption of Rare Earth Elements from Aqueous Solutions Using Geopolymers. *Proceedings* **2018**, *2*, 567. [CrossRef]
16. Cui, J.; Wang, Q.; Gao, J.; Guo, Y.; Cheng, F. The selective adsorption of rare earth elements by modified coal fly ash based SBA-15. *Chin. J. Chem. Eng.* **2022**, *47*, 155–164. [CrossRef]

17. Zhang, S.; Ravi, S.; Lee, Y.R.; Ahn, J.-W.; Ahn, W.S. Fly ash-derived mesoporous silica foams for CO_2 capture and aqueous Nd^{3+} adsorption. *J. Ind. Eng. Chem.* **2019**, *72*, 241–249. [CrossRef]
18. Aigbe, U.O.; Ukhurebor, K.E.; Onyancha, R.B.; Osibote, O.A.; Darmokoesoemo, H.; Kusuma, H.S. Fly ash-based adsorbent for adsorption of heavy metals and dyes from aqueous solution: A review. *J. Mater. Res. Technol.* **2021**, *14*, 2751–2774. [CrossRef]
19. Jadaa, W. Wastewater Treatment Utilizing Industrial Waste Fly Ash as a Low-Cost Adsorbent for Heavy Metal Removal: Literature Review. *Clean Technol.* **2024**, *6*, 221–279. [CrossRef]
20. Gadore, V.; Ahmaruzzaman, M. Tailored fly ash materials: A recent progress of their properties and applications for remediation of organic and inorganic contaminants from water. *J. Water Process. Eng.* **2021**, *41*, 101910. [CrossRef]
21. Nogueira, M.; Bernardo, M.; Ventura, M.; Matos, I.; Pinto, F.; Lapa, N. Opportunities and Constraints of the Adsorption of Rare Earth Elements onto Pyrolytic Carbon-Based Materials: A Mini-Review. *Processes* **2024**, *12*, 2257. [CrossRef]
22. Fronczak, M.; Kowalik, M.; Bystrzejewski, M. Carbon Fibers Obtained from Flax and Their Adsorption Performance in the Removal of Cu(II) and Co(II) from Aqueous Solutions. *ChemistrySelect* **2018**, *3*, 8259–8269. [CrossRef]
23. Wijitkosum, S. Biochar derived from agricultural wastes and wood residues for sustainable agricultural and environmental applications. *Int. Soil Water Conserv. Res.* **2022**, *10*, 335–341. [CrossRef]
24. Zahoor, A.; Liu, X.; Liu, Y.; Liu, S.; Yi, W.; Sajnani, S.; Tai, L.; Tahir, N.; Abdoulaye, B.; Mahaveer; et al. Agricultural lignocellulose biochar material in wastewater treatment: A critical review and sustainability assessment. *Environ. Funct. Mater.* **2025**, *4*, 117–137. [CrossRef]
25. Zhang, Y.; Zhang, X.; Zhou, Z.; Liu, G.; Wang, C. A review of the conversion of wood biomass into high-performance bulk biochar: Pretreatment, modification, characterization, and wastewater application. *Sep. Purif. Technol.* **2025**, *361*, 131448. [CrossRef]
26. Foong, S.Y.; Chan, Y.H.; Chin, B.L.F.; Lock, S.S.M.; Yee, C.Y.; Yiin, C.L.; Peng, W.; Lam, S.S. Production of biochar from rice straw and its application for wastewater remediation—An overview. *Bioresour. Technol.* **2022**, *360*, 127588. [CrossRef]
27. Zhao, Q.; Wang, Y.; Xu, Z.; Yu, Z. The potential use of straw-derived biochar as the adsorbent for La(III) and Nd(III) removal in aqueous solutions. *Environ. Sci. Pollut. Res. Int.* **2021**, *28*, 47024–47034. [CrossRef] [PubMed]
28. Awwad, N.S.; Gad, H.M.H.; Ahmad, M.I.; Aly, H.F. Sorption of lanthanum and erbium from aqueous solution by activated carbon prepared from rice husk. *Colloids Surf. B Biointerfaces* **2010**, *2*, 593–599. [CrossRef] [PubMed]
29. Zafeer, M.K.; Menezes, R.A.; Venkatachalam, H.; Bhat, K.S. Sugarcane bagasse-based biochar and its potential applications: A review. *Emergent Mater.* **2024**, *7*, 133–161. [CrossRef]
30. Lazić, B.D.; Pejić, B.M.; Kramar, A.D.; Vukčević, M.M.; Mihajlovski, K.R.; Rusmirović, J.D.; Kostić, M.M. Influence of hemicelluloses and lignin content on structure and sorption properties of flax fibers (*Linum usitatissimum* L.). *Cellulose* **2018**, *25*, 697–709. [CrossRef]
31. Zhang, L.; Fu, J.; Meng, C.; Dai, L.; Baek, N.; Gao, W.; Fan, X. Determination of the lignin content of flax fiber with the acetyl bromide-ultraviolet visible spectrophotometry method. *Text. Res. J.* **2023**, *93*, 2633–2645. [CrossRef]
32. Abd Malek, N.N.; Jawad, A.H.; Ismail, K.; Razuan, R.; ALOthman, Z.A. Fly ash modified magnetic chitosan-polyvinyl alcohol blend for reactive orange 16 dye removal: Adsorption parametric optimization. *Int. J. Biol. Macromol.* **2021**, *189*, 464–476. [CrossRef]
33. Jakubec, P.; Bartusek, S.; Dvořáček, J.J.; Šedajová, V.; Kupka, V.; Otyepka, M. Flax-Derived Carbon: A Highly Durable Electrode Material for Electrochemical Double-Layer Supercapacitors. *Nanomaterials* **2021**, *11*, 2229. [CrossRef]
34. Dizbay-Onat, M.; Vaidya, U.K.; Balanay, J.A.G.; Lungu, C.T. Preparation and characterization of flax, hemp and sisal fiber-derived mesoporous activated carbon adsorbents. *Adsorpt. Sci. Technol.* **2018**, *36*, 441–457. [CrossRef]
35. Wang, K.; Peng, N.; Sun, J.; Lu, G.; Chen, M.; Deng, F.; Do, R.; Nie, L.; Zhong, Y. Synthesis Of Silica-Composited Biochars From Alkali-Fused Fly Ash And Agricultural Wastes For Enhanced Adsorption Of Methylene Blue. *Sci. Total Environ.* **2020**, *729*, 139055. [CrossRef] [PubMed]
36. Rahman, M.M.; Karacan, I. The impact of eco-friendly chemical incorporation on the thermal oxidation process of flax fiber prior to carbonization and activation. *J. Mater. Sci.* **2022**, *57*, 2318–2333. [CrossRef]
37. Havigh, R.S.; Chenari, H.M. A comprehensive study on the effect of carbonization temperature on the physical and chemical properties of carbon fibers. *Sci. Rep.* **2022**, *12*, 10704. [CrossRef] [PubMed]
38. Tushar, M.S.H.K.; Mahinpey, N.; Khan, A.; Ibrahim, H.; Kumar, P.; Idem, R. Production, characterization and reactivity studies of chars produced by the isothermal pyrolysis of flax straw. *Biomass Bioenergy* **2012**, *37*, 97–105. [CrossRef]
39. Nurmalita, N.; Abdulmadjid, S.N.; Setiawan, A.; Idroes, R.; Jalil, Z. Characteristics of Silica Powder Extracted from Fly Ash of Coal Fired Power Plant—Effect of Heat Treatment Process. *J. Ecol. Eng.* **2023**, *24*, 282–292.
40. Radojičić, T.; Trivunac, K.; Vukčević, M.; Maletić, M.; Palić, N.; Janković-Častvan, I.; Perić Grujić, A. Rare Earth Element Adsorption from Water Using Alkali-Activated Waste Fly Ash. *Materials* **2025**, *18*, 699. [CrossRef]
41. Han, F.; Wang, L.; Li, Y.; Di, S. Application of Thermally Modified Fly Ash for Adsorption of Ni(II) and Cr(III) from Aqueous Solution: Equilibrium, Kinetic, and Thermodynamic Studies. *Environ. Eng. Sci.* **2017**, *34*, 508–515. [CrossRef]

42. Chen, C.; Cheng, T.; Zhang, X.; Zhang, M.; Lv, R. Surface modification of fly ash spheroidal particles and their application in the adsorption of phosphorus and chromium(vi) from single and competitive solute systems. *Environ. Prot. Eng.* **2020**, *46*, 39–59. [CrossRef]
43. Oliveira, L.C.A.; Pereira, E.; Guimaraes, I.R.; Vallone, A.; Pereira, M.; Mesquita, J.P.; Sapag, K. Preparation of activated carbons from coffee husks utilizing $FeCl_3$ and $ZnCl_2$ as activating agents. *J. Hazard. Mater.* **2009**, *165*, 87–94. [CrossRef]
44. Li, G.; Ye, R.; Wu, S.; Liu, X.; Huang, M.; Guo, J.; Gao, Y.; Chen, W.; Ma, Y. Fly ash-doped biochar fabricated by pyrolysis and hydrothermal strategies: Characteristics and potentialities of carbon sequestration. *Carbon. Res.* **2025**, *4*, 23. [CrossRef]
45. Khiari, B.; Ibn Ferjani, A.; Azzaz, A.A.; Jellali, S.; Limousy, L.; Jeguirim, M. Thermal conversion of flax shives through slow pyrolysis process: In-depth biochar characterization and future potential use. *Biomass Convers. Biorefin* **2021**, *11*, 325–337. [CrossRef]
46. Azevedoa, A.G.S.; Streckera, K.; Barrosa, L.A.; Tonholoa, L.F.; Lombardi, C.T. Effect of Curing Temperature, Activator Solution Composition and Particle Size in Brazilian Fly-Ash Based Geopolymer Production. *Mater. Res.* **2019**, *22*, 20180842. [CrossRef]
47. Chen, K.; Lin, W.-T.; Liu, W. Effect of NaOH concentration on properties and microstructure of a novel reactive ultra-fine fly ash geopolymer. *Adv. Powder Technol.* **2021**, *32*, 2929–2939. [CrossRef]
48. Mladenović Nikolić, N.; Kljajević, L.; Nenadović, S.S.; Potočnik, J.; Knežević, S.; Dolenec, S.; Trivunac, K. Adsorption Efficiency of Cadmium (II) by Different Alkali-Activated Materials. *Gels* **2024**, *10*, 317. [CrossRef]
49. Pearson, R.G. Hard and Soft Acids and Bases. *J. Am. Chem. Soc.* **1963**, *85*, 3533–3539. [CrossRef]
50. Foo, K.Y.; Hameed, B.H. Insights into the modeling of adsorption isotherm systems. *Chem. Eng. J.* **2010**, *156*, 2–10. [CrossRef]
51. Candela, M.T.; Martín-Rodríguez, R.; Díaz-Moreno, S.; Valiente, R.; Aguado, F.; Perdigón, A.C. Adsorption of Eu^{3+} and Gd^{3+} on high-charge micas as inner-sphere complexes. *J. Colloid Interface Sci.* **2025**, *684*, 552–565. [CrossRef]
52. Cotton, S.A. Recent advances in the chemistry of scandium. *Polyhedron* **1999**, *18*, 1691–1715. [CrossRef]
53. Lin, H.; Zhang, J.; Wang, R.; Zhang, W.; Ye, J. Adsorption properties and mechanisms of geopolymers and their composites in different water environments: A comprehensive review. *J. Water Process Eng.* **2024**, *62*, 105393. [CrossRef]
54. Ramasamy, D.L.; Wojtuś, A.; Repo, E.; Kalliola, S.; Srivastava, V.; Sillanpää, M. Ligand immobilized novel hybrid adsorbents for rare earth elements (REE) removal from waste water: Assessing the feasibility of using APTES functionalized silica in the hybridization process with chitosan. *Chem. Eng. J.* **2017**, *330*, 1370–1379. [CrossRef]
55. Ramasamy, D.L.; Puhakka, V.; Doshi, B.; Iftekhar, S.; Sillanpää, M. Fabrication of carbon nanotubes reinforced silica composites with improved rare earth elements adsorption performance. *Chem. Eng. J.* **2019**, *335*, 291–304. [CrossRef]
56. Iftekhar, S.; Srivastava, V.; Sillanpää, M. Enrichment of lanthanides in aqueous system by cellulose based silica nanocomposite. *Chem. Eng. J.* **2017**, *320*, 151–159. [CrossRef]
57. Xiao, B.; Huang, L.; Huang, W.; Zhang, D.; Zeng, X.; Yao, X. Glycine functionalized activated carbon derived from navel orange peel for enhancement recovery of Gd(III). *J. Rare Earths* **2022**, *40*, 1794–1802. [CrossRef]
58. Komnitsas, K.; Zaharaki, D.; Bartzas, G.; Alevizos, G. Adsorption of Scandium and Neodymium on Biochar Derived after Low-Temperature Pyrolysis of Sawdust. *Minerals* **2017**, *7*, 200. [CrossRef]
59. Lagergren, S. Zur the oriedersogennanten adsorption geloesterstoffe, Kungliga Svenska Vetenskapsakademiens. *Handlingar* **1898**, *24*, 1–39.
60. Ho, Y.S.; Mckay, G. Pseudo-second order model for sorption processes. *Process Biochem.* **1999**, *34*, 451–465. [CrossRef]
61. Aharoni, C.; Tompkins, F.C. Kinetics of Adsorption and Desorption and the Elovich Equation. In *Advances in Catalysis*; Eley, D.D., Pines, H., Weisz, P.B., Eds.; Academic Press: New York, NY, USA, 1970; Volume 21, pp. 1–49. ISBN 978-0-12-007821-9.
62. Weber, W.J.; Morris, J.C. Removal of Biological Resistant Pollutions from Wastewater by Adsorption. In *Advances in Water Pollution Research: Proceedings of the International Conference on Water Pollution Symposium*; Pergamon Press: Oxford, UK, 1962.
63. Langmuir, I. The adsorption of gases on plane surfaces of glass, mica and platinum. *J. Am. Chem. Soc.* **1918**, *40*, 1361–1403. [CrossRef]
64. Freundlich, H. Adsorption in solutions. *J. Phys. Chem.* **1906**, *57*, 384–410.
65. Temkin, M.I. Kinetics of Ammonia Synthesis on Promoted Iron Catalysts. *Acta Physiochimica URSS* **1940**, *12*, 327–356.
66. Dubinin, M.M.; Radushkevich, L.W. Equation of the Characteristic Curve of Activated Charcoal. *Proc. Acad. Sci. USSR Phys. Chem. Sect.* **1974**, *55*, 331–333.

Disclaimer/Publisher's Note: The statements, opinions and data contained in all publications are solely those of the individual author(s) and contributor(s) and not of MDPI and/or the editor(s). MDPI and/or the editor(s) disclaim responsibility for any injury to people or property resulting from any ideas, methods, instructions or products referred to in the content.